Modeling the dynamic fracture of polymer blends processed under shear

Gavin A. Buxton and Anna C. Balazs
Department of Chemical and Petroleum Engineering, University of Pittsburgh, Pittsburgh, Pennsyluania 15261, USA
(Received 8 September 2003; revised manuscript received 3 November 2003; published 9 February 2004)

Using computational models, we examine how shearing a binary polymer melt affects the dynamic fracture mechanics of the final solid material. The phase separation of the immiscible blend under an imposed shear is simulated through the Cahn-Hilliard method, where an advection term is added to introduce the flow field. Using this model, we simulate the structural evolution of the blend and obtain the late-stage morphology of the sheared mixture. As expected, the domains are elongated in the direction of the imposed shear. We couple these morphological results with micromechanical studies. The dynamic Lattice spring model (LSM) is utilized to simulate crack propagation through the solid blend structure. The dynamic LSM consists of a network of springs that connect regularly spaced mass points; the behavior of these points is dictated by Newtonian dynamics. The model allows us to simulate crack propagation through these heterogeneous structures and determine the strength, toughness, fracture toughness, and critical *J* integral of the material. Consequently, we can correlate the relative orientation of the interfacial regions to the overall mechanical behavior of the system. We also contrast these results with findings from simulations on the unsheared samples and thereby probe the effect of processing on the performance of polymer blends.

DOI: 10.1103/PhysRevB.69.054101 PACS number(s): 61.20.Ja, 82.35.Lr, 61.25.Hq, 62.20.Mk

I. INTRODUCTION

By mixing different polymers, researchers can tailor the blend to possess the desirable properties of the individual components. For example, the toughness and processability of a brittle polymer can be improved by adding rubbery or elastomeric polymers.[1,2] Another reason for blending polymers is economic; the dilution of a relatively expensive polymer with an inexpensive one can yield a low-cost material that retains the desired properties of the high-cost component. Most polymer pairs, however, are immiscible and consequently, the blends phase separate into heterogeneous structures, with relatively narrow interfacial regions separating the different polymeric domains. To potentially improve the intermixing of the components, an imposed flow, such as a shear, is typically applied to the mixture.[1] The imposed shear also affects the morphology of the system. Specifically, shear causes the polymer domains and interfacial regions to become elongated along the direction of the flow, yielding highly anisotropic morphologies.[3,4] There is often little interfacial adhesion between the different polymers, and therefore, the interface is typically weaker than either of the bulk materials.[2] This causes polymer blends to fail through interface decohesion (debonding) and cracks propagate along the interfaces, rather than through the polymer phases.

In this paper, we integrate two distinct computational approaches to examine how shear-induced morphological changes affect the mechanical properties of the blend. To carry out these studies, we first simulate the dynamic behavior of an immiscible AB blend in both the presence and absence of an imposed shear and obtain the late-stage structures of the mixtures. The novel aspect of this study is that we then use this morphological information to simulate the dynamic crack propagation through these heterogeneous materials. By comparing the behavior of the sheared and unsheared systems, we can obtain insight into the effects of processing on the mechanical performance of the materials.

To simulate the structural evolution of the blends, we use the Cahn-Hilliard (CH) model,[5,6] a coarse-grained theory for describing spinodal decomposition in binary mixtures. This simple model captures the diffusive nature of spinodal decomposition, but neglects hydrodynamics. For high-viscosity fluids, such as polymers, hydrodynamics plays a negligible role in the evolution of the system. Thus, the CH theory provides an appropriate model for investigating structure formation in polymeric mixtures. To introduce an externally imposed velocity, an advection term is added to the basic CH model.[3,7] While the CH approach neglects details of the polymer chain architecture, the method enables large systems to be considered and is, therefore, ideal for modeling mesoscopic phenomena, such as the shear-induced orientation of the polymer domains.

In the studies described below, we carry out the CH simulations in three dimensions. These three-dimensional calculations provide us with the elongated morphologies of polymer blends processed under shear. We then use the output from our CH simulations as the input to a micromechanical model to determine the resultant mechanical properties.

To simulate the deformation and fracture of solid polymer blends, we employ a dynamic lattice spring model (LSM). LSM's consist of a network of harmonic interactions, or springs, and allow the continuum elastic behavior of materials to be captured. The stiffness of the springs can be varied localy to model the heterogeneous nature of the material. Quasistatic LSM's, where the simulation progresses through a sequence of equilibrium states, have been used to model the micromechanics of various heterogeneous systems.[8–18] In particular, three-dimensional LSM's have allowed the deformation of particulate systems[15–17] and polymer blend structures[18] to be simulated in a computationally efficient manner.

The dynamic LSM extends the quasistatic simulations by including the dynamics of mass points situated at the intersections of the springs.[19–31] Each site, or node, corresponds

to the mass of a mesoscopic unit of the material. These nodes interact in a manner that mimics the elastic response of a material. In particular, we employ a Born LSM, which has been shown to recover the governing equations for an isotropic elastic medium.[15] The dynamics of the lattice are calculated using a discrete form of Newton's equations of motion, including a linear viscous term.

The discrete nature of the LSM and the mesoscopic length scale of the model results in a micromechanical model where microscopic phenomena are neglected. In particular, the model does not account for craze formation and crazing.[32–34] However, dynamic[26,28] and quasistatic[38] LSM's have been shown to qualitatively reproduce experimental results of polymer fracture where the mesoscopic lengthscale of interest is larger than that of the microscopic fracture mechanism.

As noted above, we take the results from our morphological investigations and directly map the phase-separated structure onto our LSM simulations. In this manner, we simulate the evolution of the phase-separating polymer blend and determine the consequences of imposed shear on the fracture mechanics of the solid material.

In the following section, we detail the CH model and the dynamic Born LSM used in this study. The results are presented in Sec. III, along with relevant discussions. In the final section, we summarize our work and draw conclusions.

II. MODEL

A. Morphology model

We describe the AB polymer blend through the coarse-grained CH approach. A coarse-grained description is appropriate because the phase separation occurs on mesoscopic length scales and over time scales where details of molecular motions can be neglected. The order parameter that characterizes this system is $\Psi(\mathbf{r})$, which is the difference in concentration between the two components, $\Psi(\mathbf{r})=\Phi_A(\mathbf{r})-\Phi_B(\mathbf{r})$, where $\Phi_A(\mathbf{r})$ and $\Phi_B(\mathbf{r})$ are the local volume fractions of components A and B, respectively. The equilibrium order parameter for the A-rich (B-rich) phase corresponds to $\Psi=\Psi_{eq}(-\Psi_{eq})$ and here we take $\Psi_{eq}=1$.

The evolution of this order parameter is described by the CH equation.[5,6] In the presence of an imposed flow, the advection term, $\mathbf{v}\cdot(\nabla\Psi)$, is added to the equation,[3,7] so that the expression now reads

$$\frac{\partial\Psi}{\partial t}+\mathbf{v}\cdot(\nabla\Psi)=M\nabla^2\frac{\delta F}{\delta\Psi}+\xi, \tag{1}$$

where M is the kinetic coefficient (mobility) of the order parameter field, and ξ is the noise field (which is set to zero in this study). In the case of simple shear, the velocity field $\mathbf{v}$ in the advection term is described in the following way:[3,7]

$$v_x(\mathbf{r})=\dot{\gamma}(t)y, \quad v_y(\mathbf{r})=v_z(\mathbf{r})=0, \tag{2}$$

where $\dot{\gamma}(t)$ is the shear rate.

The local energy term adopted in the current study is given by

$$F=\int -A\ln[\cosh(\Psi)]+\frac{1}{2}\Psi^2+\frac{D}{2}(\nabla\Psi)^2\delta\mathbf{r}, \tag{3}$$

where A and D are material specific parameters and the integration is over the volume of the system.

The above CH equation is discretized and numerically solved through a cell dynamics systems (CDS) method.[39,40] The employment of CDS [rather than a conventional discretization of Eq. (1)] significantly reduces the computational expense of the simulations and thus provides a computationally efficient model of interface dynamics in phase-separating systems. The discrete equations are of the form

$$\Psi(\mathbf{r},t+1)=G[\Psi(\mathbf{r},t)]-\langle\langle G[\Psi(\mathbf{r},t)]-\Psi(\mathbf{r},t)\rangle\rangle + \tfrac{1}{2}v_x(\mathbf{r})[\Psi(r_x+1,t)-\Psi(r_x-1,t)], \tag{4}$$

where a hyperbolic tangent model is included in the function G (although the results are insensitive to this choice of map[39])

$$G[\Psi(\mathbf{r},t)]=A\tanh(\Psi)+D[\langle\langle\Psi(r,t)\rangle\rangle-\Psi(r,t)]. \tag{5}$$

In the current simulation, the parameters are assigned the following values: $A=1.3$ and $D=0.5$. The operator $\langle\langle\star\rangle\rangle$ indicates the isotropic spatial average over the neighboring nodes, and $(\langle\langle\star\rangle\rangle-\star)$ can be considered as a discrete generalization of the Laplacian. In three dimensions, the spatial average on a cubic lattice is given by

$$\langle\langle\star\rangle\rangle=\frac{6}{80}\sum_{NN}\star+\frac{3}{80}\sum_{NNN}\star+\frac{1}{80}\sum_{NNNN}\star, \tag{6}$$

where NN, NNN, and $NNNN$ represent the nearest, next-nearest, and next-next-nearest neighbors respectively.[41]

In the absence of imposed shear flow, periodic boundary conditions are imposed and the system satisfies

$$\Psi(r_x,r_y,r_z,t)=\Psi(r_x+n_xL,r_y+n_yL,r_z+n_zL,t), \tag{7}$$

where n_x, n_y, and n_z are arbitrary integers and L is the system size. However, in the presence of an applied shear, we adopt sheared boundary conditions.[42,43]

$$\Psi(r_x,r_y,r_z,t) = \Psi(r_x+n_xL+\gamma(t)n_yL,r_y+n_yL,r_z+n_zL,t), \tag{8}$$

where $\gamma(t)$ is the shear strain experienced by the system at time t. This takes into consideration that the imposed velocity at the lower boundary ($y=0$) is zero, while at the upper boundary ($y=L$) the velocity is $\dot{\gamma}(t)L$. The sheared periodic boundary conditions keep track of this disparity in imposed shear strain.

In order to quantify the structural evolution of the phase separating morphologies, we compare the domain sizes. The domain size is defined by the "broken bond" method.[44] The domain size R is approximately $L^d/\Lambda(t)$, where L^d is the volume of the system and $\Lambda(t)$ is the total interfacial area at time t. In three dimensions ($d=3$) this becomes

$$R = \frac{L^3}{N_x + N_y + N_z} \tag{9}$$

for an isotropic system, where N_x, N_y, and N_z are the number of broken bonds (pairs of nearest-neighbor sites with opposite signs of Ψ) in the x, y, and z directions, respectively.[44] However, in the anisotropic systems considered here we separate the dimensions so that, for example, $R_x = L^3/3N_x$. This enables the domain growth in different directions in the sheared systems to be compared to the isotropic domain growth in unsheared systems.

The above equations enable us to simulate the evolution of a polymer blend under imposed simple shear flow. We now detail the micromechanical model used to probe the anisotropic mechanical properties of the resultant solid polymer composite.

B. Micromechanical model

We employ a dynamic lattice spring model (LSM). The LSM is a numerical technique for discretizing linear elasticity theory and consists of a network of springs connecting regularly spaced sites, or nodes. The energy associated with the mth node is given by[15]

$$E_m = \frac{1}{2} \sum_n (\mathbf{u}_m - \mathbf{u}_n) \cdot \mathbf{M}_{mn} \cdot (\mathbf{u}_m - \mathbf{u}_n), \tag{10}$$

where the summation is over all nearest- and next-nearest-neighboring nodes. Here, $\mathbf{u}_m$ is the displacement of the mth node from its original position and $\mathbf{M}_{mn}$ is a matrix containing the force constants (stiffness) for the spring between nodes m and n. The springs have two different types of force constants, central and noncentral. The central force constant energetically penalizes spring extension, while the noncentral force constant penalizes the rotation of springs from their original orientation. The Young's modulus E and Poisson's ratio ν are related to the force constants by the following equations:[15]

$$E = \frac{5k(2k+3c)}{4k+c}, \quad \nu = -\frac{k-c}{c+4k}, \tag{11}$$

where k and c are the central and noncentral force constants, respectively.

The harmonic form of the energy in Eq. (10) results in a force term that is linearly related to the displacements. The force acting on the mth node, due to the local displacements of its neighboring nodes, is given by

$$\mathbf{F}_m = \sum_n \mathbf{M}_{mn} \cdot (\mathbf{u}_m - \mathbf{u}_n) \tag{12}$$

To capture the dynamics of this system, we must integrate Newton's equation of motion

$$M_m \frac{\partial^2 \mathbf{u}_m}{\partial t^2} = \mathbf{F}_m - \Theta \frac{\partial \mathbf{u}_m}{\partial t}, \tag{13}$$

where M_m is the mass associated with the mth node. The Stokes drag term, with coefficient Θ, accounts for dissipation through viscous damping. The most commonly used time integration algorithm is the Verlet algorithm.[45] Here, we use the velocity Verlet algorithm[46] in order to capture the velocities (necessary for including viscous damping). The velocity Verlet scheme takes the positions, velocities and accelerations at time t to obtain the same quantities at time $t + \Delta t$ in the following way:

$$\begin{aligned}
\mathbf{u}_m(t+\Delta t) &= \mathbf{u}_m(t) + \mathbf{v}_m(t)\Delta t + \tfrac{1}{2}\mathbf{a}_m(t)\Delta t^2, \\
\mathbf{v}_m\left(t + \frac{\Delta t}{2}\right) &= \mathbf{v}_m(t) + \frac{1}{2}\mathbf{a}_m(t)\Delta t, \\
\mathbf{a}_m(t+\Delta t) &= -\frac{\mathbf{F}_m(t)}{M_m} - \Theta \mathbf{v}_m\left(t + \frac{\Delta t}{2}\right), \\
\mathbf{v}_m(t+\Delta t) &= \mathbf{v}_m\left(t + \frac{\Delta t}{2}\right) + \frac{1}{2}\mathbf{a}_m(t+\Delta t)\Delta t,
\end{aligned} \tag{14}$$

where $\mathbf{v}_m$ and $\mathbf{a}_m$ are the velocity and acceleration, respectively, of the mth node. The force acting on the mth node at time t, $\mathbf{F}_m(t)$, is taken from Eq. (12), where the local displacements are also taken at time t. The mass and central force constants are taken to be unity, the noncentral force constant is set to zero (resulting in a Poisson's ratio of $\frac{1}{4}$) and the viscous damping constant Θ is set to $\frac{1}{4}$, resulting in a material where elastic waves are under-damped. The above equations allow us to capture the elastic deformation and dynamic behavior of the material.

In order to introduce material degradation, we selectively remove springs from the system. A surface is randomly created, and hence a cluster of springs that cross this surface are broken, depending upon the strain field across the surface. An example of the springs that would be removed if a surface perpendicular to the [100] direction was chosen for failure is depicted in Fig. 1. The surface is normal to the spring connecting nodes m and n and colored dark gray, while the springs that would be removed to create this surface are colored black. Neighboring springs that are not removed when creating this surface are colored light gray. We only consider fracture surfaces that are normal to springs in the system; the strain across a surface is given by the deformation of the spring relative to its undeformed length. Creating fracture surfaces (through the removal of several springs) is necessary because of the interconnectivity of the springs, as explained below.

If a load were to be applied in the x direction (the linear elastic system would therefore be strained in the x direction), springs that possess a component in the x direction would be more extended than springs that are oriented normal to the x direction. Of the springs that possess a component in the x direction, the springs in the [100] direction would be more strained than springs in the {110} directions because of their direct orientation along x. If we were to adopt a fracture criteria that simply removed individual springs, then the springs in the [100] direction would preferentially be removed first (due to their higher strain) and the material

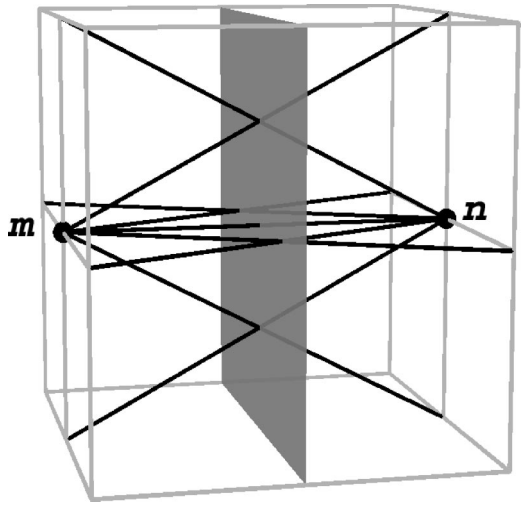

FIG. 1. The springs that would be removed upon the creation of a fracture surface normal to the [100] direction. The surface normal to the spring connecting nodes *m* and *n* is depicted as a transparent dark gray plane. The springs that would be removed upon creating the surface are colored black. Neighboring springs that are not removed upon creating the surface are colored light gray.

would remain load-bearing due to the presence of springs in the {110} directions. To avoid the creation of damaged regions that can still bear an applied load, a criteria that creates fracture surfaces through the removal of springs in both the [100] direction and the {110} directions is essential. Therefore, by creating a fracture surface through the removal of a cluster of springs, which cross a given surface, we create fracture surfaces in a more definitive and isotropic manner.

In order to determine which fracture surface is to be created a rate of failure $p_i(t)$ of a surface i at time t is introduced

$$p_i(t) \propto \left[\frac{(u_i(t) - B)}{S} \right]^{\beta}, \tag{15}$$

where $u_i(t)$ is the local strain field across the ith potential fracture surface at time t. The minimum value of strain at which fracture can occur is B, referred to as the lower bound parameter. The constant S is an arbitrary scaling parameter and the modulus β allows for a nonlinear relationship between damage rate and strain field. Assuming that the damage is to occur somewhere in the system, the probability of failure $P_i(t)$ occurring at a given surface i is the rate associated with surface i relative to the total rate of damage occurring throughout the material, i.e., $P_i(t) = p_i(t)/\Sigma_j p_j(t)$, where the sum is over all surfaces.[47] A surface is chosen to fracture from the cumulative probability and, therefore, selection takes into consideration the correct probability weightings. The cumulative probability is defined as

$$c_i(t) = \sum_{j \leq i} P_j(t) \tag{16}$$

and spans the range [0,1]. The average time interval for this failure event to occur is[47]

$$\Delta t = \frac{1}{\sum_j p_j(t)} \tag{17}$$

This time step is used to update the expressions in Eq. (14).

In order to initiate fracture, we introduce a notch, or seed crack, at the edge of the system, midway between the system boundaries and in the plane perpendicular to the applied strain. We then apply a strain field (constant displacements at the system boundaries) equivalent to 5% global strain and equilibriate the system (the nodes are moved to positions of zero force). A constant strain rate is then applied to the sample. An initial time step is introduced Δt_0 and the strain is initially increased at each iteration by $\dot{u}\Delta t_0$, where $\dot{u}$ is the constant strain rate. If the average time interval for fracture to occur [Eq. (17)] is smaller than Δt_0, then a surface is created. In particular, the ith surface chosen to fail is the surface for which $c_i(t) < RND\ [0,1] < c_{i+1}(t)$, where $RND\ [0,1]$ is a random number between 0 and 1. If the value of Δt from Eq. (17) is greater than Δt_0, then $\Delta t = \Delta t_0$, and this value is used to update the strain field and the dynamic equations with no fracture occurring. Therefore, the creation of fracture surfaces depend upon the correct probability weightings [Eq. (15)] and the relaxation of material surrounding the propagating crack tip takes into consideration the average time interval over which the crack grows. The material deforms and fractures in this manner until the crack has propagated the length of the system and two separate pieces of the material remain.

We determine the strength and toughness of the specimen from the stress-strain curve. The strength is defined as the maximum sustained stress, while the toughness is defined as the energy absorbed up to a point in the simulation where the load bearing capacity of the material is severely undermined (the stress sustained by the sample has dropped to 75% of the strength of the material).

We take the morphologies from the CH simulations and incorporate them directly into the LSM simulations. In this manner we can investigate the effects of anisotropic sheared morphologies on the ultimate strength and toughness of the material.

III. RESULTS AND DISCUSSION

We consider an incompatible AB polymer blend as it undergoes phase separation into a highly heterogeneous system. The structural evolution of this system is significantly different in the presence of shear than in the absence of this imposed flow. The blend processed under shear is shown to exhibit anisotropic morphologies. For these morphologies, we consider the mechanical properties of the resultant solid material. In particular, we simulate the propagation of a crack through the material and ascertain the strength and toughness of the sample. The mechanical properties of the sheared polymer blends are shown to exhibit significant anisotropy with respect to the direction of crack propagation.

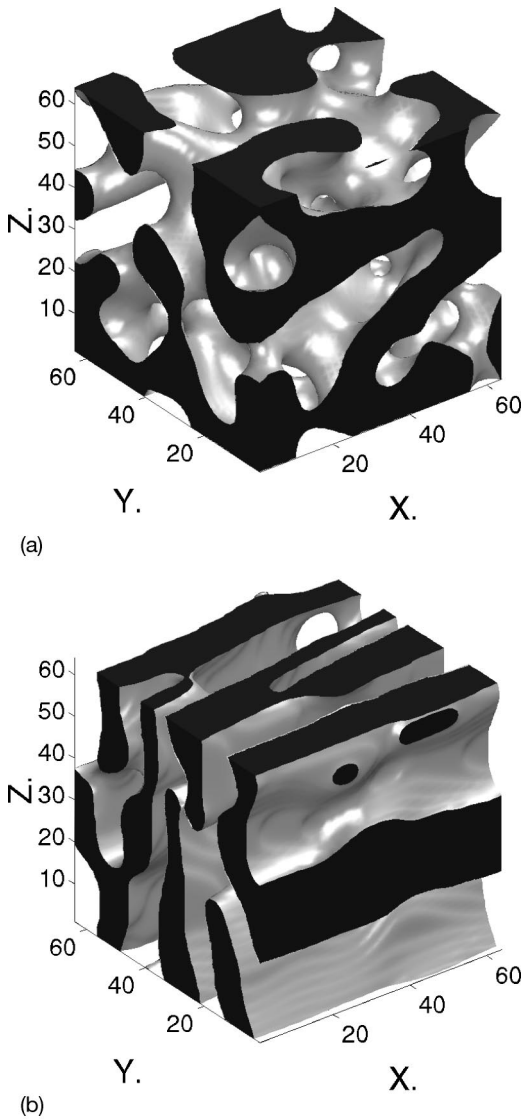

FIG. 2. Typical late-stage ($t=10\,000$) morphologies for both (a) unsheared and (b) sheared systems. Isosurfaces which separate *A*-rich regions from *B*-rich regions are colored gray.''Isocaps'' which depict where the *A*-rich regions intersect the boundaries of the simulation box are colored black.

A. Polymer blend morphologies

We contrast the structural evolution of two AB polymer blend systems; namely, one processed in the absence of an imposed flow and one processed under simple shear flow. The system size considered here is $L^3=64^3$, where L is the length of the cubic simulation box. In the case of an imposed shear, we set $\dot{\gamma}=0.0015$ in Eq. (2); this value is large enough to induce significant morphological variations, yet small enough to ensure numerical stability. Figures 2(a) and 2(b) show typical morphologies for the unsheared and sheared systems, respectively, at time $t=10\,000$, which corresponds to a relatively late-stage morphology. Isosurfaces separating *A*-rich regions (possessing a positive order parameter) and *B*-rich regions (possessing a negative order parameter) are colored gray. The black ''isocaps'' mark regions where the *A* phase intersects the boundaries of the simulation box.

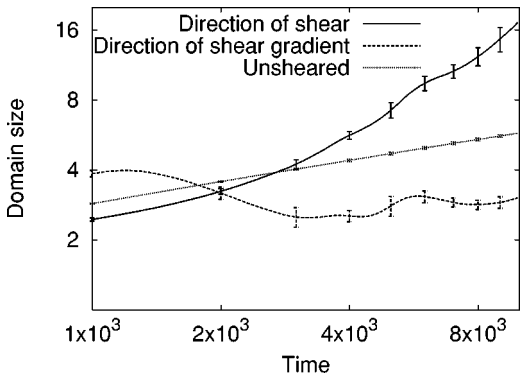

FIG. 3. Evolution of the average domain size in the direction of shear and direction of shear gradient, for the sheared systems, are compared with the average domain size for the unsheared systems.

Both sets of simulations represented in Fig. 2 begin with similar initial conditions; the order parameter is assigned values from a Gaussian distribution with a variance of 0.05. Small domains of *A* and *B* phases are formed and coarsen to form larger domains. In the absence of shear flow, these domains grow isotropically and the bicontinuous morphology shown in Fig. 2(a) emerges. However, in the presence of shear flow, the resultant morphology is no longer bicontinuous in all directions and as expected,[3,4] appears highly anisotropic [see Fig. 2(b)].

In order to quantify this anisotropy, we plot the domain size as a function of time in Fig. 3. The domain sizes are averaged over 20 independent runs and the error bars indicate the standard deviation. The domains in the unsheared system undergo an isotropic growth obeying the Lifshitz-Slyozov law,[48] where $R(t)$, the domain size, scales as $t^{1/3}$. However, the sheared domain growth is notably anisotropic. The domain growth both in the direction of shear [x direction in Fig. 2(b)] and in the direction of the shear gradient [y-direction in Fig. 2(b)] are presented in Fig. 3.

The simple shear flow considered here consists of both pure rotational and pure elongational parts. Initially, when the growth rate is more significant than the imposed shear rate, the local coalescence of domains occurs as the domains are rotated about each other. This ''tumbling'' regime causes the domain size in the direction of the shear gradient to be larger than the direction of imposed shear flow. As the growth rate decreases, the velocity difference across domains (in the direction of the shear gradient) becomes increasingly significant and the domains elongate in the direction of imposed shear. The domain size in the direction of shear becomes larger than that of the isotropic unsheared systems, while the domain size in the direction of shear gradient becomes lower. This results in highly anisotropic morphologies, such as that presented in Fig. 2(b). Similar anisotropic morphologies have been observed through comparable simulations on binary blends.[3,4,49]

The question now becomes: what are the consequences of such structural anisotropy on the mechanical properties of the solid polymeric material? We answer this question by directly mapping the morphologies from our CH simulations onto the lattice of our LSM simulations.

B. Micromechanical studies

In order to investigate the deformation and fracture of the morphologies obtained in the preceding section, we utilize a dynamic LSM. Assuming the morphologies remain unchanged as the samples are quenched to a temperature below the glass transition temperature, we can directly map a polymer melt structure from a CH lattice directly onto an unperturbed solid LSM lattice. We introduce a seed crack into the edge of the samples. As noted in the model section, we then equilibrate the system at a global deformation that corresponds to a strain of 5%. We then initiate fracture by applying an increasing strain at a constant rate (strain rate, $\dot{u} = 1.56 \times 10^{-4}$). Four fracture geometries are investigated: three corresponding to different orthogonal planes within the sheared simulations and one from the unsheared simulations. In particular, these correspond to the fracture plane being either of the following: (i) perpendicular to the direction of shear, (ii) perpendicular to the direction of the shear gradient, (iii) neutral [i.e., the x-y plane in Fig. 2(b)], or (iv) an arbitrary plane in the isotropic unsheared systems.

We are interested in the effects of anisotropy on the fracture behavior of polymer blends, and in particular, the consequence of weak interfacial regions on the strength and toughness of the material. Therefore, we keep the elastic moduli the same throughout the sample and change only the fracture criteria, making the strain-based fracture criteria for the interfacial regions 75% that of the A and B polymer domains. In this manner, we can isolate the effects of interfacial weakness on the strength and toughness of the anisotropic polymer blends. The fracture criteria is chosen so that the crack propagates continuously from the seed crack (albeit through the tortuous creation of fracture surfaces that prefer to propagate along the weak interfacial regions). We find that further reduction in interfacial fracture criteria would likely result in the decohesion of interfacial regions away from the crack tip and the subsequent growth of these cavities until final coalescence produces material failure.

The modulus of Eq. (15), determines the nonlinearity of the fracture probability. We set this equal to 4 so that regions of high strain (i.e., the crack tip) are significantly more likely to fail than regions of low strain. The lower bound constant of the interface B_I is set to 0.15, which is 75% of the lower bound constant for the A and B phases ($B_A = B_B = 0.2$). The scaling parameters are set equal to the lower bound constants. Therefore, the onset of fracture occurs at lower strains along interfacial regions than in the polymer domains. Essentially, if a region within either an A or B domain is strained by an amount $\mathbf{u}$ then the probability of fracture occurring in this region would be the same as the probability of fracture occurring in an interfacial region that is strained by an amount, $0.75 \times \mathbf{u}$.

For a case where the fracture plane is perpendicular to the direction of shear, Fig. 4 shows a typical crack propagating through the system. The fracture surface is depicted as a gray surface and can be seen to propagate in the z-x plane from the upper ($y = L$) boundary. A contour slice depicting the normal strain field (u_{xx}, where u_{ij} is the strain tensor and x is the tensile direction) is included through the middle of the sample (in the x-y plane, at $z = 32$). Figures 4(b) and 4(c) depict the propagation of the crack as it traverses the sample. The material catastrophically fails and the crack is shown to propagate through the entire material. The local normal strain field [see, for example, the strain contour in Fig. 4(b)]

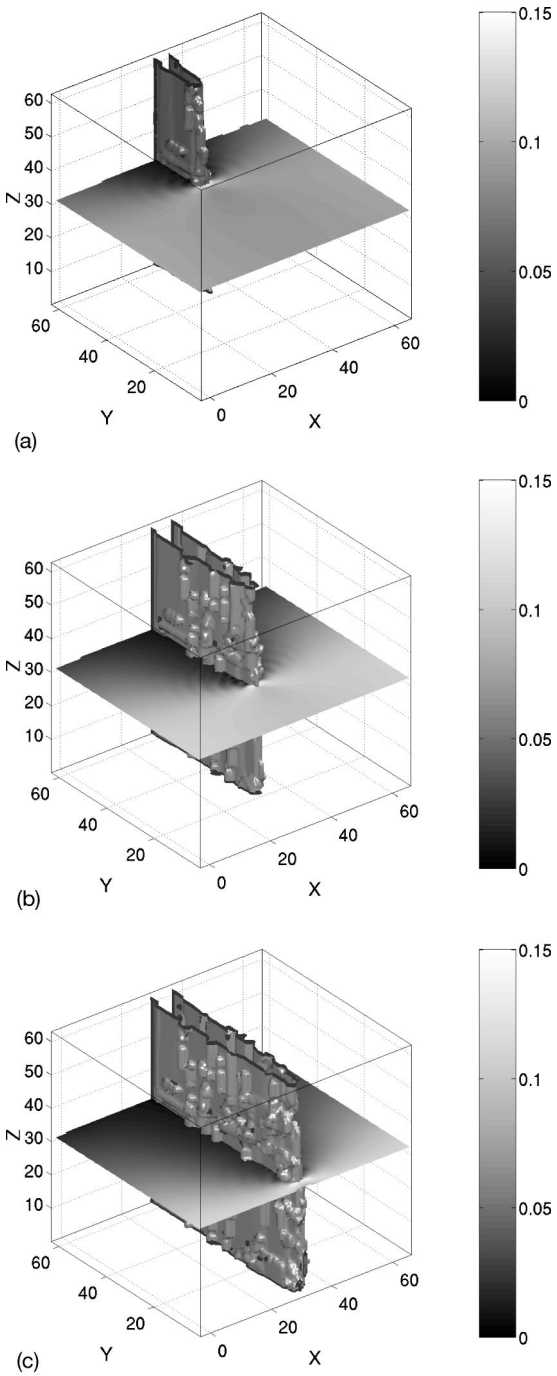

FIG. 4. A typical crack surface propagating through a system; the fracture plane is perpendicular to the direction of shear. The fracture surface is depicted as a gray surface. A contour slice depicting the normal strain field (u_{xx}, where u_{ij} is the strain tensor and x is the tensile direction) is included through the middle of the sample (in the xy plane, at $z = 32$). Different stages of crack growth are shown corresponding to (a) 2000 simulation iterations, (b) 4000 simulation iterations, and (c) 6000 simulation iterations.

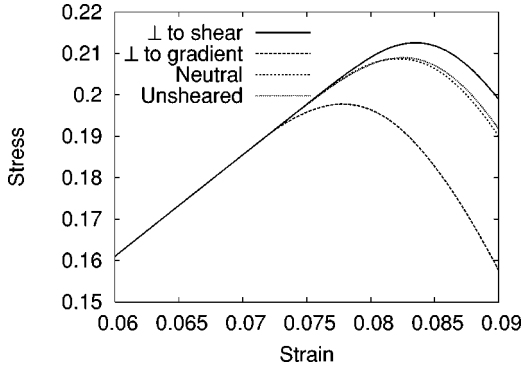

FIG. 5. Stress-strain relations for simulations where the crack propagates in all the orthogonal directions of the sheared systems and in a given direction of the unsheared systems. The data is averaged over 20 independent runs.

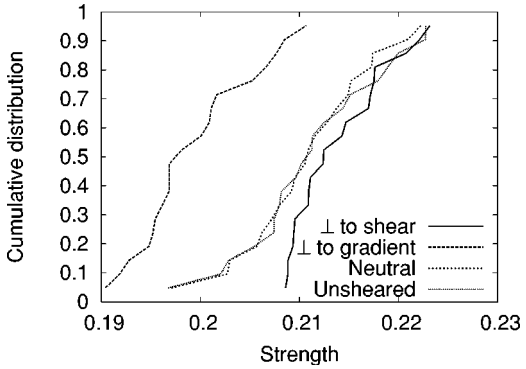

FIG. 6. Cumulative distributions of the simulation strengths where the crack propagates in all the orthogonal directions of the sheared systems and in a given direction of the unsheared systems.

depicts a maximum at the crack tip and ripples of strain intensity in the wake of the propagating crack. These ripples depict elastic waves that dissipate (due to viscous damping) as they emanate from the crack tip. Fig. 4(c) depicts the fracture surface as the crack reaches the opposite boundary from the fracture-initiating seed crack. As the crack propagates across the system there is increasing strain relaxation observed in the wake of the crack. The ability of the material to sustain stress is significantly reduced as the crack propagates across the system and this can be observed in the stress-strain relationships.

Figure 5 shows the stress-strain relations for cracks propagating in all the orthogonal directions of the sheared systems and in a given direction of the unsheared systems. The data is averaged over 20 independent runs (there is significantly high scatter in fracture results). All stress-strain relations exhibit a similar trend; as the strain is increased the gradient of the stress-strain curve reduces until it reaches zero (at the apex of the stress-strain curve) and then the stress reduces significantly in evidence of catastrophic failure. The stress-strain curves for the systems where the fracture plane is perpendicular to the shear direction ''turn over'' (the stresses sustained by the samples begin to decrease) at higher stresses, while the stress-strain curves for the systems were the fracture plane is perpendicular to the direction of the shear gradient turn over at lower stresses. Fracture through the neutral plane of the sheared samples and the arbitrary plane of the unsheared samples yield similar stress-strain curves but at intermediate values.

The strength of a sample is defined as the maximum stress that the sample can sustain. In our system, this value is taken to be the apex of the stress-strain curves. We plot the strength for all the systems considered here (twenty runs for each of the four fracture geometries considered) as cumulative distributions. The empirical cumulative distribution function (CDF) is defined as $c_i(\sigma_{max,i}) = i/n + 1$, where i is the rank of the specimen in order of increasing measured value of strength $\sigma_{max,i}$ and n is the number of samples considered. [Therefore, for $n = 20$ the empirical CDF for the lowest value of strength ($\sigma_{max,1}$) is 1/21, and for the highest value of strength ($\sigma_{max,20}$) is 20/21.] The cumulative distributions for the strengths are presented in Fig. 6. The strength of the samples fractured in the plane perpendicular to the shear direction is generally highest (to the right of the plot), while the strength of the samples fractured in the plane perpendicular to the shear gradient direction is lowest.

Similar trends are observed in the toughness data. We define the toughness to be the energy absorbed up to a point where the load bearing capacity has reduced significantly, i.e, the stress sustained by the sample is 75% of the strength. The cumulative distributions for the toughnesses are presented in Fig. 7. Similar to the strengths depicted in Fig. 6, we find that the samples fractured in the plane perpendicular to the shear direction are toughest, while the samples fractured in the plane perpendicular to the shear gradient direction are weakest.

The results presented in this paper are dimensionless, and as such, are not material specific. However, experimental fracture data is commonly presented in a manner that is material specific and not subject to the test procedure and geometry. Here, we present results from our computer simulations in an analogous, albeit dimensionless, manner. In particular, we calculate the fracture toughness and *J*-integral for both the sheared and the unsheared systems.

The stress fields at a stress concentrator (such as a precrack or notch) are dependent upon the geometry of the system and the loading stresses. However, near a blunted crack tip (due to the discrete nature of the LSM the crack tip is

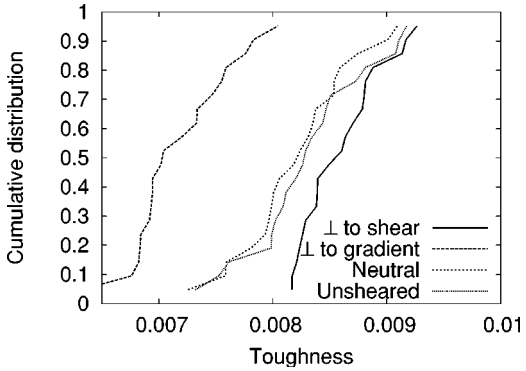

FIG. 7. Cumulative distributions of the simulation toughnesses where the crack propagates in all the orthogonal directions of the sheared systems and in a given direction of the unsheared systems.

inherently blunted), the stress fields for mode I loading (in which the crack surfaces move directly apart) can universally be obtained analytically.[50] Assuming that the load is applied in the x direction, the crack is propagating in the y direction and omitting higher-order terms, the relevant components of the stress tensor are of the form[50]

$$\sigma_{xx}=\frac{K_I}{\sqrt{2\pi r}}\left(1+\frac{\rho}{2r}\right),$$

$$\sigma_{yy}=\frac{K_I}{\sqrt{2\pi r}}\left(1-\frac{\rho}{2r}\right), \tag{18}$$

where r is the distance from the crack tip in the direction of crack propagation, ρ is the radius of the notch and K_I is the stress intensity factor for mode I loading and represents the strength of the stress fields surrounding the crack tip. The stress fields near the crack tip are only dependent upon the geometry of the system and loading conditions through the stress intensity factor. The stress intensity factor reaches a maximum value at the onset of unstable crack propagation, termed the fracture toughness, K_{Ic}. The fracture toughness is a material specific quantity and characterizes the materials resistance to failure. Given the stress fields at the onset of catastrophic failure, the fracture toughness can be obtained as

$$K_{Ic}=\frac{\sigma_{xx}\sqrt{2\pi r}}{1+\frac{\rho}{2r}}=\frac{\sigma_{yy}\sqrt{2\pi r}}{1-\frac{\rho}{2r}}. \tag{19}$$

Therefore, we can directly compare the stress fields from our computer simulations at the onset of unstable crack propagation with the result of the general analytic solution of the crack problem, thereby obtaining a value of the fracture toughness. We take ρ to be half the lattice spacing and interpolate the values of K_{Ic} from nodes away from the crack tip to the crack tip. The estimate of K_{Ic} from both the σ_{xx} and σ_{yy} components of the stress field are in excellent agreement; we present an estimate of K_{Ic} interpolated from the average of both the σ_{xx} and σ_{yy} dependent K_{Ic}'s.

The cumulative distributions of the fracture toughness data are presented in Fig. 8. In all systems considered here, 40 simulations were conducted so that the data may be fitted to a Weibull distribution (see the Appendix), allowing an estimate of the lower bound fracture toughness to be gained. Similar to the previously presented strength and toughness data, the fracture toughness of the sheared polymer system, when fractured perpendicular to the direction of shear, is generally greater than that of other systems. The fracture toughness of systems where the crack propagates perpendicular to the gradient of applied shear are for the most part found to be significantly lower than in other systems. The fracture toughness data from the systems broken in the neutral direction of the sheared systems appears to be greater than that of the unsheared system.

The J integral is a path-independent line integral that can be used to obtain an averaged measure of the near tip fields.

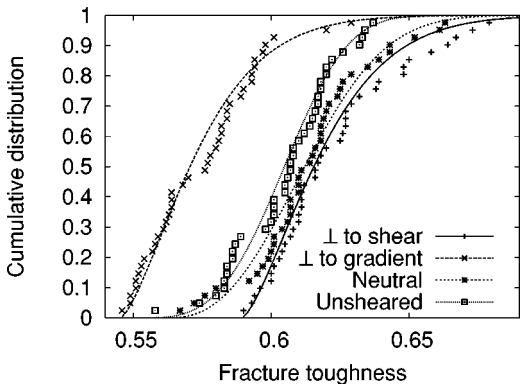

FIG. 8. Cumulative distributions of the simulation fracture toughnesses where the crack propagates in all the orthogonal directions of the sheared systems and in a given direction of the unsheared systems. Fitted Weibull curves are also depicted.

The path independence of the J integral allows data far from the crack tip to be used in calculating the fracture resistance of the system (and the fracture toughness if $\sigma_{ij}n_j\rightarrow 0$, making J synonymous with the energy release rate). The J integral is of the form[51]

$$J=\int_\Gamma (Wn_y-\sigma_{ij}n_j u_{i,y})dC, \tag{20}$$

where W is the strain energy density, **n** is the outward normal along Γ, the path of the integral, and $u_{i,y}$ represents the differentiation of the displacement field with respect to the y direction. We numerically evaluate this term using two separate paths, one that encircles the notch close to the crack tip and one that encircles the notch far from the crack tip. The critical J integral is defined as the J integral evaluated at the onset of unstable crack propagation. The difference in critical J integral J_c obtained between the two paths is always found to be less than 2%.

The cumulative distributions of the critical J integral data are presented in Fig. 9 along with Weibull fits. The J integral results are qualitatively similar to the fracture toughness data. The systems where the crack propagates perpendicular

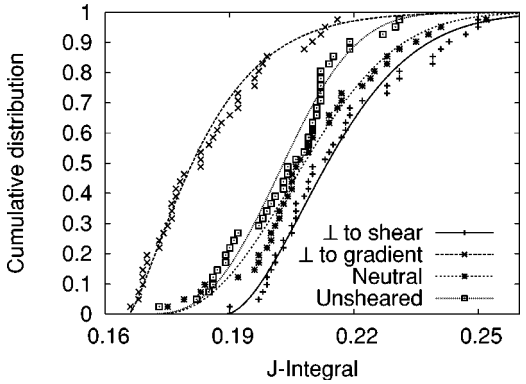

FIG. 9. Cumulative distributions of the simulation critical J-integral where the crack propagates in all the orthogonal directions of the sheared systems and in a given direction of the unsheared systems. Fitted Weibull curves are also depicted.

to the applied shear have on average a higher value of J_c than other systems considered here. On average, the lowest values of J_c were found for the system were the crack propagates perpendicular to the direction of the shear gradient. Similar to the fracture toughness data, the systems broken in the neutral direction of the sheared systems are distinguishable from that of the unsheared systems, and are typically found to possess greater values of J_c.

The lower bound fracture toughness and *J* integral can be obtained from the location parameter of the Weibull distributions (see the Appendix). The lower bound fracture toughness is a safety criteria for engineering materials, indicating the minimum stress intensity factor a material can be subjected to while still ensuring material integrity. The lower bound fracture toughnesses and *J* integrals in the systems considered here are presented in the following table

System	K_{Ic}	J_c
$\perp$ to shear	0.589	0.189
$\perp$ to gradient	0.545	0.166
neutral	0.562	0.172
unsheared	0.552	0.170

The general trends of the lower bound data are similar to the general responses given in Figs. 8 and 9 (perpendicular to shear is greatest and perpendicular to gradient is lowest). In Figs. 8 and 9, the systems that were fractured perpendicular to the shear gradient were found to be significantly weaker than the other systems considered (which gave marginally different distributions). However, the lower bound fracture toughnesses and *J* integrals reveal that systems fractured perpendicular to the applied shear possess significantly greater values than the other systems, all of which possess lower bound values that are close.

In the sheared morphologies, larger domain sizes were found in the direction of applied shear than in the unsheared system. A large domain size indicates few broken bonds in this direction [see Eq. (9)] and, hence, fewer interfacial regions that would have to be fractured to create a fracture surface perpendicular to this direction. As interfacial regions are weaker in our investigations, fewer interfacial regions oriented parallel to the fracture plane correspond to a stronger and tougher material. In contrast, smaller domain sizes were found in the direction of shear gradient, and therefore, a greater number of broken bonds were in this direction. This results in a greater concentration of interfacial regions that would decohere as a crack propagates perpendicular to this direction and, hence, ultimately a weaker material.

IV. SUMMARY AND CONCLUSIONS

We investigate the three-dimensional phase separation of an AB polymer blend processed in the presence and absence of an imposed, simple shear. The effects of the imposed shear become more pronounced as the domain growth slows down. As expected, we find that the sheared morphologies become highly anisotropic. Relative to the unsheared system, the imposed flow elongates the domains in the direction of the shear. With this morphological data as input, we then investigate the fracture mechanics of the sheared and unsheared polymer blends.

In particular, we investigate the propagation of cracks through the heterogeneous blend. To encourage crack propagation along the interface between the *A* and *B* domains, the fracture probability of interfacial regions is greater than the fracture probability in either the *A* or *B* domains. We observe that crack propagation in the sheared system exhibits anisotropic mechanical properties. The strength and toughness of samples fractured in a plane perpendicular to the direction of applied shear flow are superior to other samples considered here. In contrast, samples fractured in a plane perpendicular to the direction of the shear gradient are found to be weaker.

These findings indicate that the orientation of the interfaces in polymer blends has a significant impact on the mechanical properties of the material. Interfaces oriented parallel to the fracture plane (perpendicular to the tensile direction) provide an easy path for the crack to follow, and hence, result in macroscopically weaker materials. Furthermore, we found that sheared systems can provide better mechanical stability than unsheared systems.

Through the integration of a morphological model and a micromechanical model we have related the processing conditions of a polymer melt to the ultimate strength and toughness of the solid material. The predictive capabilities of such an integrated approach can aid in the design of new materials, and facilitate the use of polymer blends in engineering structures.

APPENDIX

Here we describe how the Weibull distribution[52] (common in fracture mechanics) can be ''fitted'' to statistical data. The cumulative distribution function is of the form

$$c(x) = 1 - \exp\left[-\left(\frac{x-a}{b} \right)^m \right], \tag{A1}$$

which upon differentiation results in the following probability density function

$$p(x) = \frac{m}{b}\left(\frac{x-a}{b} \right)^{m-1} \exp\left[-\left(\frac{x-a}{b} \right)^m \right], \tag{A2}$$

where b is the scale parameter, m is the Weibull modulus, and a is the location parameter. The method of maximum-likelihood estimation is adopted in order to provide an unbiased and uncorrelated fit.[53]

The maximum-likelihood method consists of taking as the estimators those values of the parameters that maximize the likelihood of the observations.[54] The likelihood of a single observation is given by $p(x_i)$, where x_i is the ith observation. The likelihood of a series of observations is given by $\Lambda = \Pi_{\langle i \rangle} p(x_i)$. Computationally, however, it is more convenient for the logarithm of the likelihood to be considered. The maximum likelihood is obtained through the differentiation of $\ln\Lambda$ with respect to the parameters.

The two-parameter Weibull distribution is obtained through the substitution of $t_i = x_i - a$, therefore removing the functional dependence upon the location parameter; the sub-

sequent solution is consequently a function of the initial value of a. The logarithm of the likelihood is of the form

$$\ln\Lambda = N\ln\left(\frac{m}{b}\right) + \sum_{\langle i\rangle}\left[(m-1)(\ln t_i - \ln b)\right] + \sum_{\langle i\rangle}\left[-\left(\frac{t_i}{b}\right)^m\right], \tag{A3}$$

where N is the number of data points.

The differentiations, with respect to the parameters m and b, are given as

$$\frac{\partial \ln\Lambda}{\partial m} = \frac{N}{m} + \sum_{\langle i\rangle}(\ln t_i - \ln b) - \sum_{\langle i\rangle}\left[\left(\frac{t_i}{b}\right)^m \ln\left(\frac{t_i}{b}\right)\right], \tag{A4}$$

$$\frac{\partial \ln\Lambda}{\partial b} = -\frac{Nm}{b} + \frac{m}{b}\sum_{\langle i\rangle}\left[\left(\frac{t_i}{b}\right)^m\right]. \tag{A5}$$

Maximization is obtained by setting the above equations to zero, giving the following relations[53]

$$F(m) = \frac{N}{m} + \sum_{\langle i\rangle}\ln t_i - N\frac{\sum_{\langle i\rangle}(t_i^m \ln t_i)}{\sum_{\langle i\rangle} t_i^m} = 0, \tag{A6}$$

$$\frac{dF(m)}{dm} = -\frac{N}{m^2} - N\frac{\left[\sum_{\langle i\rangle} t_i^m\right]\left[\sum_{\langle i\rangle} t_i^m (\ln t_i)^2\right]}{\left[\sum_{\langle i\rangle} t_i^m\right]^2} + N\frac{\left[\sum_{\langle i\rangle}(t_i^m \ln t_i)\right]^2}{\left[\sum_{\langle i\rangle} t_i^m\right]^2}. \tag{A7}$$

The Newton-Raphson method is used to obtain the optimum estimator of m (for which both the function and its derivative are required[55]), which upon substitution into Eq. (A5), gives the estimate for b. The constants m and b are therefore obtainable, as a function of a, and the estimation of a is now obtained using the bisection method.

In order to estimate the location parameter, the following derivative is considered

$$\frac{\partial \ln\Lambda}{\partial a} = -(m-1)\sum_{\langle i\rangle}\frac{1}{x_i - a} + \sum_{\langle i\rangle}\frac{m}{b}. \tag{A8}$$

Upon setting this equation to zero, it can be solved through the bisection method.[55] The location parameter represents the lower bound of the distribution.

[1] G.R. Strobl, *The Physics of Polymers* (Springer-Verlag, Berlin, 1996).
[2] L.H. Sperling, *Polymeric Multicomponent Materials* (Wiley-Interscience, New York, 1997).
[3] T. Ohta, H. Nozaki, and M. Doi, J. Chem. Phys. **93**, 2664 (1990).
[4] F. Corberi, G. Gonnella, and A. Lamura, Phys. Rev. Lett. **81**, 3852 (1998).
[5] J.W. Cahn and J.E. Hilliard, J. Chem. Phys. **28**, 258 (1958).
[6] J.W. Cahn, J. Chem. Phys. **42**, 93 (1965).
[7] T. Ohta, Y. Enomoto, J.L. Harden, and M. Doi, Macromolecules **26**, 4928 (1993).
[8] K.A. Snyder, E.J. Garcozi, and A.R. Day, J. Appl. Phys. **72**, 5948 (1992).
[9] L. Monette, M.P. Anderson, S. Ling, and G.S. Grest, J. Mater. Sci. **27**, 4393 (1992).
[10] L. Monette and M.P. Anderson, Scripta metall. et Mater. **28**, 1095 (1993).
[11] L. Monette, M.P. Anderson, and G.S. Grest, J. Appl. Phys. **75**, 1155 (1994).
[12] L. Monette, M.P. Anderson, H.D. Wagner, and R.R. Mueller, J. Appl. Phys. **75**, 1442 (1994).
[13] M. Ostoja-Starzewski, P.Y. Sheng, and I. Jasuik, Eng. Fract. Mech. **58**, 581 (1997).
[14] K. Alzebdeh, A. Al-Ostaz, I. Jasuik, and M. Ostoja-Starzewski, Int. J. Solids Struct. **35**, 2537 (1998).
[15] G.A. Buxton, C.M. Care, and D.J. Cleaver, Modell. Simul. Mater. Sci. Eng. **9**, 485 (2001).
[16] G.A. Buxton and A.C. Balazs, J. Chem. Phys. **117**, 7649 (2002).
[17] G.A. Buxton and A.C. Balazs, Phys. Rev. E **67**, 031802 (2003).
[18] G.A. Buxton and A.C. Balazs, Interface Sci. **11**, 175 (2003).
[19] M. Marder and X. Liu, Phys. Rev. Lett. **71**, 2417 (1993).
[20] T.T. Rautiainen, M.J. Alava, and K. Kaski, Phys. Rev. E **51**, R2727 (1995).
[21] P. Heino and K. Kaski, Phys. Rev. B **54**, 6150 (1996).
[22] T.T. Rautiainen, M.J. Alava, and K. Kaski, Phys. Rev. E **56**, 6443 (1997).
[23] J. Astrom and J. Timonen, Phys. Rev. Lett. **78**, 3677 (1997).
[24] P. Heino and K. Kaski, Phys. Rev. E **56**, 4364 (1997).
[25] J. Astrom, M. Alava, and J. Timonen, Phys. Rev. E **57**, R1259 (1998).
[26] O. Pla, F. Guinea, E. Louis, S.V. Ghaisas, and L.M. Sander, Phys. Rev. B **57**, R13 981 (1998).
[27] O. Pla, F. Guinea, E. Louis, S.V. Ghaisas, and L.M. Sander, Phys. Rev. B **61**, 11 472 (2000).
[28] T. Martín, P. Espa˜nol, M.A. Rubio, and I. Zú˜niga, Phys. Rev. E **61**, 6120 (2000).
[29] P. Szelestey, P. Heino, J. Kertész, and K. Kaski, Phys. Rev. E **61**, 3378 (2000).
[30] A. Politi and M. Zei, Phys. Rev. E **63**, 056107 (2001).
[31] S. Fratini, O. Pla, P. Gonzalez, F. Guinea, and E. Louis, Phys. Rev. B **66**, 104104 (2002).
[32] P. Beahan, M. Bevis, and D. Hull, Philos. Mag. **24**, 1267 (1971).
[33] P. Beahan, M. Bevis, and D. Hull, J. Mater. Sci. **8**, 162 (1972).
[34] Crazes are microscopic regions of polymeric material where the polymer has been drawn out from the bulk in the form of fibrils. These fibrils span across the crack tip and allow the crack to bear an applied load. The lattice spacing in the LSM is considered to be larger than the crazed microstructure and therefore the model does not capture crazing. Crazing has been included into lattice models through the introduction of special anisotropic

regions of the lattice (Refs. 35–37), although this requires the initial specification of crack direction (something that is problematic in heterogeneous materials).

[35] C.Y. Hui, A. Ruina, C. Creton, and E.J. Kramer, Macromolecules **25**, 3948 (1992).

[36] Y. Sha, C.Y. Hui, A. Ruina, and E.J. Kramer, Macromolecules **28**, 2450 (1995).

[37] Y. Sha, C.Y. Hui, A. Ruina, and E.J. Kramer, Acta Mater. **45**, 3555 (1997).

[38] M. Vujesevic and D. Krajcinovic, Int. J. Solids Struct. **34**, 1105 (1997).

[39] Y. Oono and S. Puri, Phys. Rev. Lett. **58**, 836 (1987).

[40] Y. Oono and S. Puri, Phys. Rev. A **38**, 434 (1988).

[41] A. Shinozaki and Y. Oono, Phys. Rev. E **48**, 2622 (1993).

[42] A.W. Lees and S.F. Edwards, J. Phys. C **5**, 1921 (1972)

[43] M. Doi and D. Chen, J. Chem. Phys. **90**, 5271 (1989).

[44] T. Ohta, D. Jasnow, and K. Kawasaki, Phys. Rev. Lett. **49**, 1223 (1982).

[45] L. Verlet, Phys. Rev. **159**, 98 (1967).

[46] M. Tuckerman, B.J. Berne, and G.J. Martyna, J. Chem. Phys. **97**, 1990 (1992).

[47] W.A. Curtin, M. Pamel, and H. Scher, Phys. Rev. B **55**, 12 051 (1997).

[48] M. Lifshitz and V.V. Slyozov, J. Phys. Chem. Solids **19**, 35 (1961).

[49] F. Corberi, G. Gonnella, and A. Lamura, Phys. Rev. E **62**, 8064 (2000).

[50] H. Tada, *The Stress Analysis of Cracks Handbook* (Del Research Corporation, Hellertown, 1973).

[51] J.R. Rice, J. Appl. Mech. **35**, 379 (1968).

[52] W. Weibull, J. Appl. Mech. **18**, 293 (1951).

[53] A. Ghosh, Comput. Geosci. **25**, 729 (1999).

[54] J. A. Rice, *Mathematical Statistics and Data Analysis* (Wadsworth and Brooks/Cole, Pacific Grove, CA, 1988).

[55] W. H. Press, B. P. Flannery, S. A. Teukolsky, and W. T. Vetterling, *Numerical Recipes in C: The Art of Scientific Computing* (Cambridge University Press, Cambridge, 1988).